The bulge masses of TDE host galaxies and their scaling with black hole mass

Paige Ramsden[1]★, Daniel Lanning[1], Matt Nicholl[1,2], Sean L. McGee[1]
[1]School of Physics and Astronomy, University of Birmingham, Birmingham B15 2TT, UK
[2]Institute for Gravitational Wave Astronomy, University of Birmingham, Birmingham B15 2TT, UK

Accepted XXX. Received YYY; in original form ZZZ

arXiv:2201.02650v1 [astro-ph.HE] 7 Jan 2022

ABSTRACT

Tidal disruption events (TDEs) provide a means to probe the low end of the supermassive black hole (SMBH) mass distribution, as they are only observable below the Hills mass ($\lesssim 10^8 M_\odot$). Here we attempt to calibrate the scaling of SMBH mass with host galaxy bulge mass, enabling SMBH masses to be estimated for large TDE samples without the need for follow-up observations or extrapolations of relations based on high-mass samples. We derive host galaxy masses using PROSPECTOR fits to the UV-MIR spectral energy distributions for the hosts of 29 well-observed TDEs with BH mass estimates from MOSFIT. We then conduct detailed bulge/disk decomposition using SDSS and PanSTARRS imaging, and provide a catalog of bulge masses. We measure a positive correlation between SMBH and bulge mass for the TDE sample, with a power-law slope of 0.28 and significance $p = 0.06$ (Spearmans) and $p = 0.05$ (Pearsons), and an intrinsic scatter of 0.2 dex. Applying MC resampling and bootstrapping, we find a more conservative estimate of the slope is 0.18 ± 0.11, dominated by the systematic errors from PROSPECTOR and MOSFIT. This is shallower than the slope at high SMBH mass, which may be due to a bias in the TDE sample towards lower mass BHs that can more easily disrupt low-mass stars outside of the event horizon. When combining the TDE sample with that of the high mass regime, we find that TDEs are successful in extending the SMBH - stellar mass relationship further down the mass spectrum and provide a relationship across the full range of SMBH masses.

Key words: transients: tidal disruption events – galaxies: nuclei – black hole physics

1 INTRODUCTION

Supermassive black holes (SMBHs) exist within the nuclei of most galaxies and their properties couple with those of their hosts. The measured mass of the central SMBH correlates with the galaxy's bulge mass, luminosity and stellar velocity dispersion (e.g. Gebhardt et al. 2000; Häring & Rix 2014; Ferrarese & Ford 2005). These scaling relationships are thought to indicate SMBH influence on the formation and evolution of the galaxies that they lie within. If the slope can be well constrained, such relations make it possible to estimate the masses of large samples of SMBHs, enabling studies from early structure formation to the evolution of SMBHs (Gültekin et al. 2009; Kormendy & Ho 2013; McConnell & Ma 2013a). However, as direct SMBH measurements are most commonly available for massive active galactic nuclei (AGN) and a handful of very nearby systems, the commonly-used relationships are calibrated only by samples that are dominated by SMBHs more massive than $\gtrsim 10^7\,M_\odot$ (e.g. Kormendy & Ho 2013; Bentz et al. 2013).

However, at least one important physical phenomenon is restricted to SMBHs of lower mass: tidal disruption events (TDEs) of stars (Hills 1975; Rees 1988). If a star is unlucky enough to pass too close to a SMBH, tidal forces outweigh the binding energy of the star and so it is torn apart. This occurs at the 'tidal radius',

$$R_T = \left(\frac{M_{\rm BH}}{M_*}\right)^{\frac{1}{3}} R_* \quad (1)$$

for a black hole of mass $M_{\rm BH}$ and a star of mass M_* and radius R_*. If this occurs outside of the event horizon of the black hole,

$$R_G = \frac{2GM_{\rm BH}}{c^2}, \quad (2)$$

approximately half of the disrupted material falls back onto the SMBH, likely forming an accretion disk, while the other half becomes unbound (Rees 1988; Lacy & Townes 1982). Both the circularization and ultimate accretion of the bound matter can cause a luminous flare, with characteristic luminosity of $\sim 10^{44}$erg s^{-1} (Rees 1988; Gezari 2021). However, if the tidal radius is smaller than the gravitational radius of the SMBH, the star's orbit will intersect the event horizon before disruption, and so it will be swallowed whole, without a visible flare (Hills 1975; MacLeod et al. 2012). The requirement $R_T > R_G$ introduces a critical SMBH mass, called the Hills mass, to produce an observable a TDE. This is $\lesssim 10^8 M_\odot$ for a star of $\sim 1 M_\odot$, or $\lesssim 10^7 M_\odot$ for a more common star of ~ 0.1M. Therefore, observations of TDEs offer a new opportunity to probe lower-mass black holes, identifying those that may otherwise lie dormant and undetected, and enabling us

★ Contact e-mail: pxr754@alumni.bham.ac.uk

© 2021 The Authors

to study their evolution at lower parts of the mass function (Mockler et al. 2019; Wevers et al. 2017).

TDEs are now found routinely by wide-field, time-domain surveys, such as the Panoramic Survey Telescope and Rapid Response System (Pan-STARRS; Kaiser et al. (2010)), the Zwicky Transient Facility (ZTF; Bellm et al. (2019)), the Asteroid Terrestrial Impact Last Alert System (ATLAS; Tonry et al. (2018)) and the All-Sky Automated Survey for Supernovae (ASASSN; Kochanek et al. (2017)). They can be differentiated from other luminous transients by a lack of colour evolution; a long rise time and fade time relative to most supernovae (SNe); and a power-law decline from the peak, relatively consistent with the classic $t^{-5/3}$ prediction (Rees 1988; Hung et al. 2018; van Velzen et al. 2021). Distinct spectroscopic features include a colour temperature of $10,000 - 50,000$ K and broad emission lines of H I, He II and N III (Gezari et al. 2012; Arcavi et al. 2014; Blagorodnova et al. 2019; van Velzen et al. 2021). Most recently, 17 new TDEs were discovered by ZTF and studied by van Velzen et al. (2021). With the upcoming Vera Rubin Observatory and its Legacy Survey of Space and Time (LSST; Ivezić et al. 2019), and the Extended Roentgen Survey with an Imaging Telescope Array (eROSITA; Khabibullin et al. 2013), it is predicted that this field will be further revolutionised by the detection of thousands of TDEs per year (Stone & Metzger 2015; Bricman & Gomboc 2020; Khabibullin et al. 2013).

The most precise BH mass estimates require the orbital velocity distribution of stars and/or gas close to the galactic nucleus (Kormendy & Ho 2013), which can only be measured spectroscopically. It will not be possible to obtain spectroscopic BH mass measurements for such a large sample of TDEs, yet such masses would be extremely valuable in understanding TDE properties, and in building a picture of SMBHs at the low end of their mass function. Assuming the TDE luminosity is 'prompt', i.e. its evolution follows the fallback rate of material (Guillochon et al. 2018), the TDE light curve can be modelled directly to derive dynamical quantities of the encounter, including SMBH mass (Mockler et al. 2019; Stone & Metzger 2015). Yet even this method requires high-cadence, multiwavelength follow-up of each TDE, due to the limited cadence of LSST and the fact that TDEs emit most of their energy in the UV. This method too becomes impractical for studying ~ 1000 TDEs.

However, the majority of future TDEs will have excellent host galaxy imaging from their discovering surveys: LSST will achieve final depths of $\sim 26 - 27$ mag in stacked images. If the BH masses in TDE host galaxies correlate with properties that can be measured photometrically, constructing the TDE BH mass function can be done essentially "for free". It is known that SMBH masses correlate with the luminosity, or equivalently the mass, of their host galaxies, and in particular correlate with the mass of the inner bulge at a significance comparable to their correlation with velocity dispersion (Gültekin et al. 2009; Kormendy & Ho 2013; McConnell & Ma 2013a). However, this relation has been calibrated mainly at BH masses too large to produce a TDE (e.g. Wevers et al. 2019), so it has been unclear if it applies, or differs, in the TDE regime $M_{\rm BH} \sim 10^6\,M_\odot$.

Moreoever, TDEs occur in unusual galaxies, where the slope of a BH–galaxy correlation could differ. They are over-represented in quiescent Balmer-strong galaxies, otherwise called post-starburst or E+A galaxies. These galaxies are defined by distinct Balmer line absorption and weak, or no, emission lines (French et al. 2016; Arcavi et al. 2014; Graur et al. 2018; Law-Smith et al. 2017). This is suggestive of low levels of current star-formation (the lack of emission lines), but with substantial activity in the last ~Gyr (Balmer absorption from A-type stars) (French et al. 2016; Zabludoff et al. 1996). French et al. (2016) found that quiescent Balmer-strong galaxies host more than one third of the observed sample of TDEs, yet they make up only 0.2% of local galaxies. It is possible that these are post-merger galaxies (Zabludoff et al. 1996), resulting in an enhanced TDE rate caused by the interaction of two SMBHs (Chen et al. 2009). Enhancement of the TDE rate could also be caused by the formation of quiescent Balmer-strong galaxies via galaxy interaction, unique stellar populations existing in the cores of the galaxies (Arcavi et al. 2014), or by high central stellar densities (Graur et al. 2018).

Armed with the growing sample of known TDEs and an ever increasing discovery rate, now is the time to confirm whether TDEs can pick out low mass SMBHs, identify whether BH masses obtained from light curve fits are reliable, and extend the calibration of SMBH-host relations to the TDE regime. In this study, we derive host galaxy bulge masses for a sample of 29 TDEs using pre-flare photometry from optical, UV and IR sky surveys, in combination with the stellar population synthesis code Prospector (Leja et al. 2017), and bulge-to-total light (B/T) ratios measured by decomposing SDSS and PanSTARRS host galaxy images.

SMBH masses for these events have been estimated using mosfit (companion paper by M. Nicholl et al.), and we use these to derive the SMBH–bulge mass relation for the TDE sample. Combining these data with the well-studied high-mass end of the SMBH mass function, we attempt to measure the slope of the SMBH–stellar mass relation from $\lesssim 10^6\,{\rm M}_\odot$ to $\gtrsim 10^{10}\,{\rm M}_\odot$. We find a moderately significant correlation within the TDE host population, but compared to the high-mass sample it is weaker, with larger intrinsic scatter and a flatter slope. This may be the result of systematic difficulties in measuring their SMBH masses, but could also reflect the bias towards low-mass SMBHs due to event horizon suppression.

In Section 2, we present the selection of TDE candidates and their host galaxies, alongside a description of the Prospector model used and choice of priors. Results for galaxy mass are displayed and compared with previous literature, and B/T ratios are used to find the galaxy bulge masses. In Section 3 the BH–bulge mass for the TDE sample is analysed and results are reported with their significance. Finally, the TDE sample is combined with that of the high mass regime (Kormendy & Ho 2013) and the SMBH–bulge mass relationship is derived for the whole range of SMBH masses. The paper ends with discussion and conclusions in Section 4.

2 SPECTRAL ENERGY DISTRIBUTION FITS AND BULGE MASSES

2.1 Data Sample

The sample of TDEs were selected based on the work of van Velzen et al. (2021), resulting in an up to date (2020) initial sample of 39 well observed events from recent ZTF data and previous literature. Of these, 32 have BH mass measurements from Nicholl et al (in preparation) using the Mosfit TDE model[1] (Mockler et al. 2019). To derive host galaxy masses, we require (at minimum) multicolour optical imaging of the host, either from a previous study of the TDE in question or from a wide-field survey like PanSTARRS or SDSS. Three southern hemisphere TDEs (OGLE16aaa, ASASSN-18ul/AT2018fyk, ASASSN-18pg/AT2018dyb) did not pass this cut. The final sample utilised 15 (of 17) ZTF TDEs and 14 (of 22) literature TDEs. These are listed in Table 1.

[1] BH mass estimates for many of these events are available elsewhere in the literature (e.g. Wevers et al. 2019), however using any galaxy-based estimates would make our analysis circular.

Table 1. Our sample of 29 TDEs with their locations, redshifts and the derived host galaxy bulge masses.

IAU Name/Discovery Name	RA	Decl.	Redshift (z)	Classification reference	$\log(M_{\rm bulge}/M_{\odot})$
AT2018zr	07:56:54.530	+34:15:43.61	0.071	Tucker et al. (2018)	$9.95^{+0.10}_{-0.10}$
AT2018hco	01:07:33.635	+23:28:34.28	0.090	van Velzen et al. (2018)	$9.99^{+0.09}_{-0.10}$
AT2018iih	17:28:03.930	+30:41:31.42	0.212	van Velzen et al. (2021)	$10.54^{+0.10}_{-0.15}$
AT2018hyz	10:06:50.871	+01:41:34.08	0.046	Dong et al. (2018)	$9.15^{+0.09}_{-0.11}$
AT2018lna	07:03:18.649	+23:01:44.70	0.091	van Velzen et al. (2019b)	$9.36^{+0.13}_{-0.14}$
AT2019cho	12:55:09.210	+49:31:09.93	0.193	van Velzen et al. (2021)	$9.87^{+0.13}_{-0.20}$
AT2019bhf	15:09:15.975	+16:14:22.52	0.121	van Velzen et al. (2021)	$10.28^{+0.12}_{-0.15}$
AT2019azh	08:13:16.945	+22:38:54.03	0.022	van Velzen et al. (2019c)	$10.11^{+0.08}_{-0.07}$
AT2019dsg	20:57:02.974	+14:12:15.86	0.051	Nicholl et al. (2019b)	$10.07^{+0.10}_{-0.11}$
AT2019ehz	14:09:41.880	+55:29:28.10	0.074	Gezari et al. (2019)	$9.73^{+0.12}_{-0.17}$
AT2019eve	11:28:49.650	+15:40:22.30	0.064	van Velzen et al. (2021)	$9.25^{+0.09}_{-0.10}$
AT2019mha	16:16:27.799	+56:25:56.29	0.148	van Velzen et al. (2021)	$9.75^{+0.08}_{-0.08}$
AT2019meg	18:45:16.180	+44:26:19.21	0.152	van Velzen et al. (2019a)	$10.14^{+0.12}_{-0.27}$
AT2019lwu	23:11:12.305	- 01:00:10.71	0.117	van Velzen et al. (2021)	$9.58^{+0.09}_{-0.09}$
AT2019qiz	04:46:37.880	- 10:13:34.90	0.015	Siebert et al. (2019)	$9.47^{+0.10}_{-0.12}$
GALEX-D1-9	02:25:17.00	- 04:32:59.00	0.326	Gezari et al. (2006)	$10.40^{+0.11}_{-0.11}$
GALEX-D3-13	14:19:29.81	+52:52:06.37	0.370	Gezari et al. (2008)	$10.99^{+0.17}_{-0.16}$
SDSS-TDE1	23:42:01.41	+01:06:29.30	0.136	van Velzen et al. (2011)	$10.14^{+0.12}_{-0.19}$
SDSS-TDE2	23:23:48.62	- 01:08:10.34	0.252	van Velzen et al. (2011)	$10.40^{+0.12}_{-0.16}$
PS1-10jh	16:09:28.28	+53:40:23.99	0.170	Gezari et al. (2012)	$9.64^{+0.12}_{-0.18}$
PS1-11af	09:57:26.82	+03:14:00.94	0.405	Chornock et al. (2014)	$10.07^{+0.16}_{-0.13}$
PS17dhz/AT2017eqx	22:26:48.30	+17:08:52.40	0.109	Nicholl et al. (2019a)	$9.51^{+0.11}_{-0.14}$
PTF-09ge	14:57:03.18	+49:36:40.97	0.064	Arcavi et al. (2014)	$10.08^{+0.10}_{-0.10}$
PTF-09djl	16:33:55.97	+30:14:16.65	0.184	Arcavi et al. (2014)	$10.31^{+0.13}_{-0.15}$
ASASSN-14ae	11:08:40.12	+34:05:52.23	0.043	Holoien et al. (2014)	$9.73^{+0.15}_{-0.17}$
ASASSN-14li	12:48:15.23	+17:46:26.44	0.021	Holoien et al. (2016a)	$9.78^{+0.07}_{-0.07}$
ASASSN-15oi	20:39:09.18	- 30:45:20.10	0.020	Holoien et al. (2016b)	$8.91^{+0.10}_{-0.08}$
iPTF-16axa	17:03:34.34	+30:35:36.60	0.108	Hung et al. (2017)	$10.07^{+0.11}_{-0.11}$
iPTF-16fnl	00:29:57.01	+32:53:37.24	0.016	Blagorodnova et al. (2017)	$9.81^{+0.05}_{-0.07}$

Broadband photometry of TDE host galaxies, prior to the point of disruption, was obtained through survey catalogue searches and collated to construct spectral energy distributions (SEDs). Optical data in the u, g, r, i, z, y[2] bands were collected from SDSS and PanSTARRS. From SDSS, the default 'model Mags' were used, while aperture magnitudes were retrieved from PanSTARRS. Near-infrared (NIR) and mid-infrared (MIR) data were collected from the 2MASS and WISE catalogues, via the NASA/IPAC Infrared Science Archive, whilst UV data was collected from the GALEX catalogue via VizieR. From 2MASS, the extended profile-fit magnitudes (m_{ext}) were retrieved for J, H and K_s bands. NUV and FUV bands were obtained from GALEX where possible. The default WISE photometry (instrumental standard aperture magnitude) was used for all hosts, except those that are larger in projection than the default 8.25 arcsecond aperture. This occurred most commonly for TDEs at redshifts of $z \sim 0.02$. In this case we used WISE galaxy-fitting photometry if available, otherwise larger apertures were queried. All photometric data have been homogenised within the AB magnitude system.

Due to the lower resolution of WISE, issues with blending were identified. Any data that appeared to be anomalously bright in the WISE bands was investigated using higher resolution optical images from PanSTARRS or SDSS. If two or more sources were identified within the image it was assumed that blending had occured and the WISE data was removed. Blending was not considered an issue for optical/NIR bands due to much smaller point spread functions (PSFs), and was not an issue for GALEX due to a reduced number of UV-bright sources compared to IR.

[2] u bands from SDSS, y bands from PanSTARRS

2.2 SED Fits

Modelling of the SED of each galaxy was conducted using Prospector (Leja et al. 2017), with all fits run on the University of Birmingham's bluebear high performance computing cluster. Prospector uses the Flexible Stellar Population Synthesis (FSPS) package (Conroy et al. 2009) and creates synthetic spectra for stellar populations. The modelled SED is the total of a galaxy's content: stars and gas. Within this work, we adopted the same model used by Nicholl et al. (2020) to analyse the host of the TDE AT2019qiz, which is an implementation of Prospector-α (Leja et al. 2017). The model free parameters used were stellar mass, defined as the mass of existing stars and stellar remnants (Leja et al. 2017); stellar metallicity; a six component star-formation history (SFH); and three parameters which control the dust fraction and reprocessing.

van Velzen et al. (2021) previously modelled the SEDs of the same sample of galaxies, also using Prospector, but included only optical and UV data and assumed a parametric SFH. It is important to note that, in this paper, a non-parametric SFH is used, which enables a better understanding of the age of the system (Leja et al. 2017). Furthermore, the stellar population age is degenerate with mass and metallicity, hence a more accurate constraint on this will allow for a more reliable extraction of host galaxy mass (Leja et al. 2017). The number of SFH bins, as well as size and location, has

Table 2. Statistical values obtained via data analysis for both the isolated TDE sample and combined sample. Values resulting from systematic errors added in quadrature are also shown. Resampling refers to the bootstrapping + perturbation method detailed in section 3.1 **Note:** any zero values shown represent p-value (and errors) that tend to zero. These values are ≤ 0.05.

		Pearson Coeff (r_p)	Pearson P-val (P_p)	Spearman Coeff (r_s)	Spearman P-val (P_s)	Gradient	y-intercept
TDE sample	Simple fit	0.38	0.05	0.35	0.06	0.28	3.82
	Resampling	$0.34^{+0.08}_{-0.00}$	$0.08^{+0.11}_{-0.05}$	$0.33^{+0.09}_{-0.09}$	$0.13^{+0.10}_{-0.10}$	$0.26^{+0.07}_{-0.07}$	$4.00^{+0.66}_{-0.67}$
	Resampling+systematic	$0.24^{+0.14}_{-0.00}$	$0.20^{+0.38}_{-0.16}$	$0.23^{+0.15}_{-0.15}$	$0.31^{+0.33}_{-0.27}$	$0.18^{+0.11}_{-0.11}$	$4.83^{+1.04}_{-1.07}$
Combined TDE + high mass sample	Simple fit	0.86	< 0.001	0.82	< 0.001	1.34	-6.33
	Resampling	$0.84^{+0.01}_{-0.00}$	< 0.001	$0.81^{+0.01}_{-0.01}$	< 0.001	$1.31^{+0.03}_{-0.03}$	$-6.06^{+0.31}_{-0.31}$
	Resampling+systematic	$0.82^{+0.02}_{-0.00}$	< 0.001	$0.79^{+0.02}_{-0.02}$	< 0.001	$1.24^{+0.05}_{-0.05}$	$-5.33^{+0.53}_{-0.52}$

to be balanced between minimising computational resources and maximising amount of SFH information obtained. As described in Leja et al. (2017), we used a six component SFH which includes the current star-formation rate (sSFR) and five equal-mass bins for SFH.

Use of the stellar metallicity free parameter is important as it plays a key role in derivation of ages, dust attenuation and masses, due to its influence on the optical-to-NIR ratio (Bell & de Jong 2001; Mitchell et al. 2013). The final three dust parameters relate to the optical depth from general interstellar dust within the galaxy and how this depth varies with wavelength, plus the optical depth of any additional dust in star-forming regions as a fraction of the average. Further discussion of these parameters can be found in Leja et al. (2017). In this paper, we focus on the results for stellar mass and marginalise over all other parameters; analysis of other derived properties, in particular the SFHs, will be the subject of a follow-up study.

Prospector produces well-sampled posterior probability distributions for each of the detailed model parameters using Markov chain Monte Carlo (MCMC) analysis, via the emcee package (Foreman-Mackey et al. 2013). This also allows us to marginalise over the various model parameters in order to obtain reliable mass measurements with realistic error bars that account for degeneracies between parameters. All 29 SEDs are presented in Appendix A. All derived free parameters, including the galaxy mass (and bulge ratio described in section 2.3), are given in Appendix B. The final galaxy bulge masses are presented in Table 1. For the TDE sample, we find bulge masses in the range of $10^{8.91} - 10^{10.99} M_{\odot}$, with a median of $10^{9.95} M_{\odot}$.

The galaxy masses measured are comparable with previous literature. We find that our well-sampled total stellar mass values are systematically, slightly larger than previous measurements. In Graur et al. (2018), galaxy stellar masses were computed with the LePhare code (Ilbert et al. 2009) and SDSS ugriz cmodel magnitudes (Stoughton et al. 2002). We found that, when fitting SEDs containing only archival photometry from SDSS our data was in complete agreement with Graur et al. (2018), whilst when fitting SEDs with the full wavelength range from UV to NIR/MIR our results were typically larger. Similarly, van Velzen (2018) used photometric data from SDSS and 2MASS to estimate stellar mass via kcorrect (Blanton & Roweis 2007). Again we find that our data results in larger total stellar masses. Even more relevant, a comparison to van Velzen et al. (2021) indicates the same result. As previously mentioned, van Velzen et al. (2021) used only optical and UV data, primarily from SDSS, and assumed a parametric SFH, but they also used the Prospector code. When comparing results on host galaxy total stellar mass, we find that while values generally agree within 1-σ, on average our results are systematically larger, typically by ~ 0.3 dex. In combination, these comparisons suggest that previous measurements may have been underestimates due to a reduced amount of archival photometry used.

2.3 Bulge decomposition

The decomposition of TDE host galaxy light into both a bulge and disk component was done using profit (Robotham et al. 2017). This *R* package models the two-dimensional photometric profile of a galaxy within a Bayesian framework and therefore produces well-justified model uncertainties. The galaxy profiles were determined using g-band images from both the SDSS and PanSTARRS surveys. For each image, a Moffat function (Moffat 1969) was fit to the nearest 10 unsaturated bright stars, the result of which was used as the point spread function for the fitted galaxy light profile. The Moffat function is commonly used as an analytic approximation to the point spread function, and contains the Gaussian function as a limiting case, but allows for the possibility of broader wings in the distribution. Nonetheless, our results are not sensitive to the choice of the functional form of the PSF.

For each image, a segmentation map was made using sextractor (Bertin & Arnouts 1996). These segmentation maps are used by profit during the modelling process to avoid contributions of light profiles from nearby sources and to properly compute the noise level in the image. With profit, we modelled the galaxy light as the combination of a de Vaucouleur bulge component (Sersic index n=4) and an exponential disk component (Sersic index n=1). For each of the bulge and the disk components, there were 6 fitted parameters: x and y central coordinate, magnitude, effective radius, orientation of the major axis, and axial ratio (minor-axis/major-axis). These components were fitted in log space with uniform priors using the Bayesian optimisation scheme from LaplacesDemon with the maximum likelihood galaxy model solution from the BFGS algorithm (Fletcher 1970) as an initial starting point. Ultimately, the bulge-to-total ratio is the ratio of the computed bulge magnitude to the total (bulge+disk) magnitude and the results are listed in Table B1, Appendix B. In 24 cases, the B/T was computed from the SDSS g image, and for the remaining 5 cases from the PanSTARRS g image. When both images were available, the computed B/T agreed very well (B/T_{SDSS} - $B/T_{PanSTARRS}$ = 0.034 ± 0.072).

3 THE BH - BULGE MASS RELATION

3.1 Data Analysis Methods

In order to identify correlations between our data, we utilised both the Pearson Correlation Coefficient r_p and the Spearman Rank Correlation Coefficient r_s, testing the strength of linear and monotonic relationships respectively. The slope of an assumed power-law relation (e.g. Kormendy & Ho 2013) was determined through the best-fit straight line in $\log M_{\rm BH} - \log M_{\rm bulge}$, and was calculated using standard χ^2 minimisation.

Monte Carlo (MC) sampling techniques were used to account for limitations within our data sets. To ensure any correlation was not driven by a few extreme values, we first applied a bootstrapping method. Within each iteration, N data points were selected randomly with replacement ($N = 29$ being the number of data points in total). These were then resampled within their errors by approximating each drawn point as a 2D Gaussian distribution using the 1σ widths of the Prospector posteriors and Mosfit posteriors. When including systematic errors in the analysis, these widths included a systematic error of 0.32 dex in galaxy mass, taken from the average difference between our masses and those for the same objects in van Velzen et al. (2021) and Graur et al. (2018), and a systematic error of 0.20 in the SMBH mass (from Mockler et al. 2019), respectively. This approach, termed 'bootstrapping + perturbation' by Curran (2014), captures both the size of the errors and the effects of a finite sample size.

The best fit gradients and intercepts, the statistical coefficients r_p and r_s and their p-values were calculated at each step. Each posterior was explored in full over 50,000 iterations, and probability distributions for each of the 6 statistical values were produced. Table 2 presents all values obtained via statistical analysis methods described, with and without including the estimated systematic errors.

3.2 TDE Sample

SMBH mass as a function of host galaxy bulge mass for the TDE sample is illustrated in Figure 1. With no resampling, we find a Spearman coefficient $r_s = 0.35$ with a significance of $P_s = 0.06$. The best-fit straight line, which we call the 'simple' fit, has a gradient of 0.28 and a y-intercept of 3.82. Expressed in the same form as Kormendy & Ho (2013), this gives a relationship between SMBH mass and host galaxy bulge mass:

$$\frac{M_{\rm BH}}{10^9 M_\odot} = 0.01 \left(\frac{M_{\rm Bulge}}{10^{11} M_\odot}\right)^{0.28} . \quad (3)$$

On the same plot, we show the results after applying the MC resampling alongside bootstrapping with replacement, with the average fit shown as a green line. If we consider only the statistical errors in the data, we calculate a Spearman coefficient of $r_s = 0.33^{+0.09}_{-0.09}$ with a significance of $P_s = 0.13^{+0.10}_{-0.10}$. A correlation is usually considered significant only if $p < 0.05$. From this fitting procedure we see that approximately 32% of trials were formally significant, suggestive of a possible positive correlation at moderate statistical significance for this sample. If we include also the systematic errors on each parameter (Leja et al. 2017; Mockler et al. 2019), we instead find, $r_s = 0.23^{+0.15}_{-0.15}$ with a significance of $P_s = 0.31^{+0.33}_{-0.27}$. However, when looking at the percentage of significant trials via MCMC fitting, it remains that approximately 15% of trials were significant despite the limitations of the large systematic errors.

The bootstrapping + perturbation best fit, illustrated in Figure 1, has a gradient of $0.26^{+0.07}_{-0.07}$ (without systematic errors), or $0.18^{+0.11}_{-0.11}$ if we include the estimated systematics. The most conservative relationship between SMBH mass and host galaxy bulge mass was therefore found to lie within the 1σ range

$$\frac{M_{\rm BH}}{10^9 M_\odot} = (0.01^{+0.01}_{-0.02}) \cdot \left(\frac{M_{\rm Bulge}}{10^{11} M_\odot}\right)^{(0.18\pm0.11)} . \quad (4)$$

In order to determine how well BH masses can be derived using the relationship, the intrinsic scatter of the data around this line was calculated. We used the method of McConnell & Ma (2013b) (their equation 4), taking into account the statistical and systematic errors in each parameter, and varying the intrinsic scatter term for each fit until $\chi^2 = 1$ was achieved. We find that the intrinsic scatter of the data around equation 4 is 0.22 dex. If we instead use the slope from equation 3, we find a scatter of 0.20 dex. In summary, these equations can be used to estimate the SMBH masses of TDE hosts from their bulge masses to within around 0.2 dex.

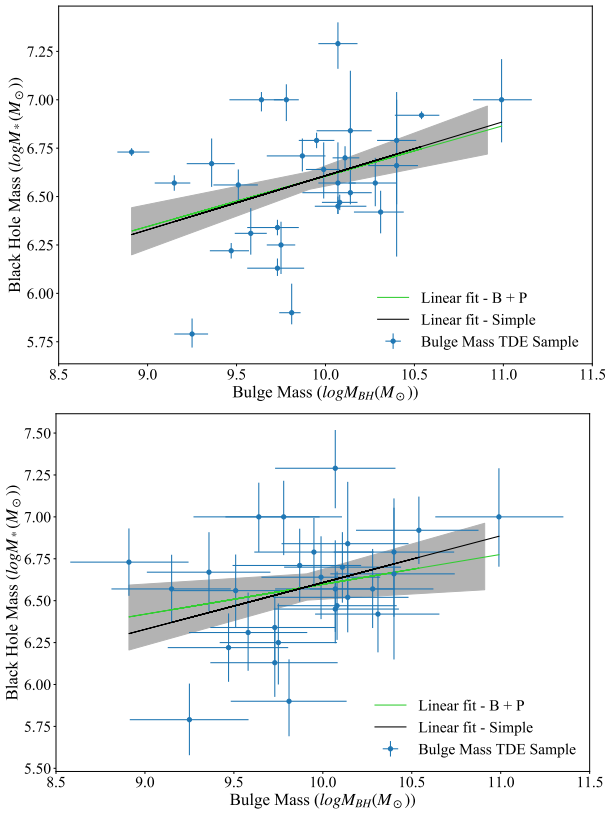

Figure 1. SMBH mass as a function of host galaxy bulge mass, with a basic fit to the correlation in black. The green line and grey region represent the median and 90% confidence interval calculated through Bootstrapping and Perturbation (P + B) of the data. The top panel includes only our derived statistical errors, while the bottom includes estimates of the systematic error on each quantity from mosfit and prospector. The black line corresponds to equation 3, while the green line in the lower panel corresponds to equation 4.

3.3 TDE Sample in Combination with High-mass Regime

In order to determine where TDEs and their hosts fall within the mass distributions of other SMBH samples, and whether they can improve the calibration of the SMBH–stellar mass relationship at the low end of the mass spectrum, the TDE sample was combined with

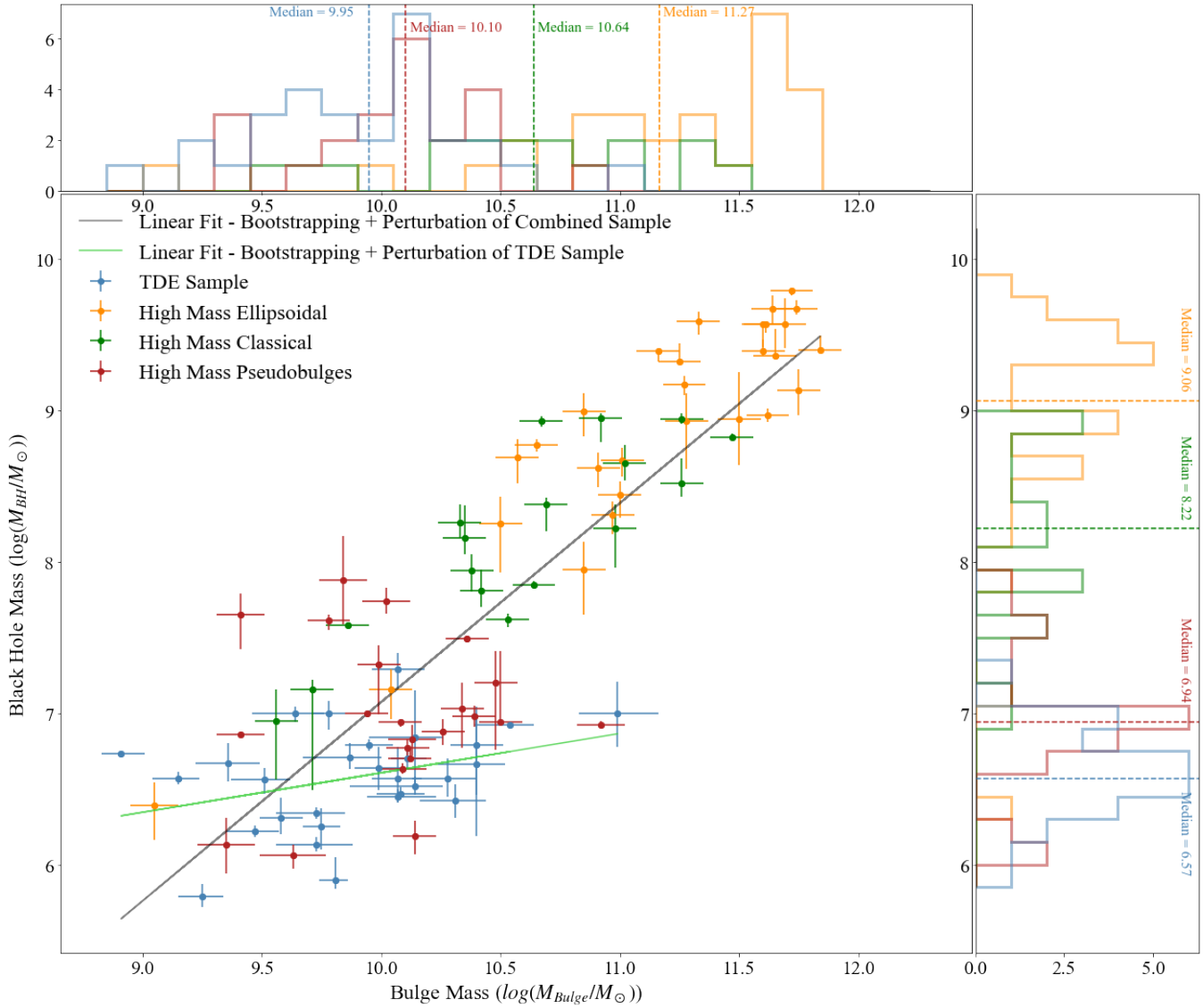

Figure 2. SMBH mass as a function of host galaxy bulge mass for the TDE sample (blue, showing statistical errors only) and the high-mass regime: ellipsoidal galaxies (orange), classical bulges (green) and pseudobulges (red). The black line (equation 5) shows the averaged fit to the combined sample, after bootstrapping and MC resampling, while the green line shows the equivalent quantity for the TDEs only (equation 4). Histograms of the bulge and SMBH mass distributions are shown on their respective axes, where the median of each distribution is indicated via a dashed line.

that of the high-mass regime. We used the data from Kormendy & Ho (2013), which is sourced from an inventory of host galaxies with SMBH measurements based on stellar dynamics, maser disk dynamics, ionized gas dynamics, or CO molecular gas disk dynamics. The inventory was categorised into morphological types: elliptical galaxies, classical bulges and pseudobulges. The data in total comprise 67 sources. We omitted any data that Kormendy & Ho (2013) neglected to fit, and any sources that they identified as ongoing mergers.

Figure 2 shows SMBH mass as a function of host galaxy bulge mass for the combined sample. TDE host galaxies have the lowest SMBH and bulge masses, and populate the previously sparsely-filled region of the plot with $M_{\rm bulge} \lesssim 10^{10}\,{\rm M}_\odot$ and $M_{\rm BH} \lesssim 10^{7}\,{\rm M}_\odot$. We apply the same statistical tests to this sample as in the previous section. Unsurprisingly, given the known correlation in the high-mass sample, the combined sample is found to have a strong correlation with $p \ll 0.05$.

The gradient derived from the MC sampling and bootstrapping, illustrated in Figure 2 but including systematic errors, is $1.31^{+0.03}_{-0.03}$, with a y-intercept of $-6.06^{+0.31}_{-0.31}$. The best fit relationship across the whole sample was therefore found to be

$$\frac{M_{\rm BH}}{10^9 M_\odot} = (0.22^{+0.27}_{-0.26}) \cdot \left(\frac{M_{\rm Bulge}}{10^{11} M_\odot}\right)^{(1.24\pm0.05)} \quad (5)$$

4 DISCUSSION

Compared to other methods of measuring BH mass, we find that TDEs can be used to directly target low mass SMBHs. The median SMBH mass found for our TDE sample is $10^{6.57}\,{\rm M}_\odot$ (Nicholl et al, in preparation) compared to the median of the high mass regime

$10^{8.07}$ M$_\odot$. This supports the idea that observations of lower mass SMBHs ($\sim 10^6$ M$_\odot$) are more common around TDEs, due to the critical mass resulting from the the tidal and gravitational radius inequality, $R_T > R_S$ (Hills 1975). Here we have demonstrated that these are also found in galaxies with low bulge masses, $\lesssim 10^{10.5}\,M_\odot$

The scaling of SMBH mass with host galaxy mass identified in our isolated TDE sample was statistically weaker than the very strong correlation found in the combined sample. Shown in Figure 2, the TDE sample visibly populates the lower half of the combined relationship, extending it to lower mass BHs. There is significant overlap between pseudobulges and our TDE sample, with the median pseudobulge SMBH mass laying much closer to that of the TDEs than the other components of the high mass regime. Kormendy & Ho (2013) removed the pseudobulge sample from their final relationship after concluding they did not satisfy the tight SMBH–host galaxy correlations that classical and elliptical bulges did.

For our purposes, the pseudobulge sample are interesting to consider due to their greater overlap in SMBH mass with the TDE hosts (Kormendy & Ho 2013). As a general definition, pseudobulges are bulges which have morphologies reminiscent of disk galaxies – as opposed to classical bulges, which appear similar to elliptical galaxies (Fisher & Drory 2008; Kormendy & Ho 2013). When fitted with a Sérsic profile, pseudobulges have a lower index, n_b, indicating a smaller bulge (Fisher & Drory 2008) which, considering co-evolution, suggests a lower mass SMBH. Furthermore, Hu (2008) found that pseudobulges have a tight SMBH–velocity dispersion relation, but with a slope that is distinct from that measured in the classical bulges and elliptical galaxies. This suggests that SMBH growth in pseudobulges is slower than that in the early-type bulges (Hu 2008; Kormendy & Ho 2013). While they have been previously omitted from the SMBH–stellar mass relationship, with the addition of the TDE sample, it is clear that pseudobulges do fit within the combined sample. This further indicates the successful role TDEs play in extending the relationship to the lower mass end of the SMBH spectrum.

Comparing the final extended SMBH - stellar mass relationship derived for the combined sample, equation 5, to that derived in Kormendy & Ho (2013),

$$\frac{M_{\rm BH}}{10^9 M_\odot} = (0.49^{+0.06}_{-0.05}) \left(\frac{M_{\rm Bulge}}{10^{11} M_\odot}\right)^{1.16\pm0.08} \tag{6}$$

we see that the normalisation is in $\sim 1\sigma$ agreement, but the difference in the exponent is significant. Moreover, the exponent we derived is $\sim 5\sigma$ away from being linear, compared to the $\sim 2\sigma$ difference in Kormendy & Ho (2013). Therefore, with the combined sample we find a steeper SMBH–stellar mass relationship, indicative of a faster scaling SMBH mass. It is worth noting that while Kormendy & Ho (2013) omitted pseudobulges in their final relationship due to finding a reduced correlation between SMBHs, when removing pseudobulges from our combined sample there are no significant changes in the statistical values shown in Table 2.

Although we have extended the mass range, we are not claiming that our measured relationship is more reliable than the widely used relation from Kormendy & Ho (2013). In particular, the faster scaling in our sample relies on the accuracy of the SMBH mass measurements from Nicholl et al., and hence are limited by the approximations used in light curve modelling. However, the indicative results from our study suggest that if we can obtain accurate SMBH masses for future large TDE samples, these will have significant statistical power in constraining the slope of this fundamental relationship.

The comparative flatness between the TDE-only and combined samples could be due to a restrictive and small sample size for the TDEs. The TDE sample obtained is a good representation of all observed TDEs, but covers narrow ranges of SMBH ($10^{5.80}$ – $10^{7.37}$ M$_\odot$) and host galaxy bulge masses ($10^{8.91}$ – $10^{10.99}$ M$_\odot$). Recovering a correlation with substantial intrinsic scatter is difficult with only a small dynamic range. However, it is also possible that this shallower correlation is a true physical effect of the TDE sample; it could be caused by the bias TDEs have towards lower mass BHs due to the limiting Hills mass (Hills 1975). In addition, it can be seen in Figure 2, between a fixed bulge mass of 10^{10} M$_\odot$ – 10^{11} M$_\odot$, that the TDE SMBH masses are systematically lower than those of the elliptical and classical samples, by ~ 1 dex. This further highlights the bias that TDEs have towards lower mass SMBHs. A larger sample is required to further understand the difference in relation in this crucial mass range.

It is predicted that TDE observations will be revolutionised by upcoming surveys; the current detection rate of 10 year^{-1} is set to increase to thousands year^{-1} (Bricman & Gomboc 2020; Khabibullin et al. 2013). Covering $\sim$ 10,000 deg^2 of sky each night, the upcoming LSST will survey six optical bands over 10 years, visiting each field approximately 900 times. Using the LSST simulation framework, Bricman & Gomboc (2020) predicted that LSST will discover between 35,000 - 80,000 TDEs during the survey. A large fraction will not have sufficient follow-up data for detailed individual study. However, the host galaxy information provided by LSST will be excellent, even with no targeted follow-up, due to the unprecedented survey depth. Hence, utilising the derived relationship between TDE host galaxy bulge mass and BH mass will allow us to efficiently analyse the upcoming sample. Given the narrow mass range of TDE hosts and the offset in SMBH masses for hosts in the range 10^{10} – 10^{11} M$_\odot$, we suggest to use the TDE-only relation to estimate SMBH masses for these events. This is accurate to ~ 0.2 dex which is smaller than the systematic offset compared to the Kormendy & Ho (2013) relation. In time, the larger TDE sample will also enable us to improve the calibration of the SMBH–stellar mass relationship for TDEs, using those LSST events which are sufficiently well-observed for independent BH mass estimates.

5 CONCLUSIONS

We have modelled photometric data of 29 TDE host galaxies, deriving the total stellar mass and bulge mass for each event. The SMBH–stellar mass relationship was investigated for both the TDE sample and the TDE sample combined with that of the high-mass regime from Kormendy & Ho (2013). Our main conclusions are as follows:

- TDEs are successful in providing direct measurements of low mass SMBHs, with a median observed SMBH mass of $10^{6.57}$ M$_\odot$ compared to $10^{8.07}$ M$_\odot$ for previous SMBH samples.
- We find bulge masses in the range of $10^{8.91}$ – $10^{10.99}\,M_\odot$ with a median of $10^{9.95}$ M$_\odot$.
- We find a correlation between TDE host SMBH and bulge masses, with moderate statistical significance. The simple best-fit relation has a power-law slope of 0.28. After applying statistical tests and considering systematic errors, we show that the slope lies in the range 0.18 ± 0.11 (1σ) and the relation has an intrinsic scatter of 0.2 dex.
- The relative flatness of this relation is different from that seen at higher SMBH mass, possibly reflecting event horizon suppression of the TDE rate.
- Combining the TDE sample with higher mass SMBHs, the

strong positive correlation between bulge and SMBH mass is unsurprisingly recovered. However, TDEs prove to be highly constraining of the slope at the low mass end, and our sample shows possible evidence for a faster scaling of SMBH mass with bulge mass than previous studies, warranting further investigation with future large samples.

Our results indicate that TDEs are promising future probes for low mass SMBHs. With the projected detection rate of thousands per year, TDEs present an opportunity to explore a population of low-mass SMBHs that may otherwise lay dormant in the centre of their galaxies. The sample of TDEs and their hosts will continue to grow, enabling further understanding of the relationships and co-evolution between them.

ACKNOWLEDGEMENTS

We thank Joel Leja for helpful discussions about systematic uncertainties in the stellar population systhesis. MN is supported by funding from the European Research Council (ERC) under the European Union's Horizon 2020 research and innovation programme (grant agreement No. 948381) and by a Fellowship from the Alan Turing Institute.

DATA AVAILABILITY

This article is based on existing publicly available data.

REFERENCES

Arcavi I., et al., 2014, The Astrophysical Journal, 793, 38
Bell E. F., de Jong R. S., 2001, The Astrophysical Journal, 550, 212
Bellm E. C., et al., 2019, Publications of the Astronomical Society of the Pacific, 131, 068003
Bentz M. C., et al., 2013, ApJ, 767, 149
Bertin E., Arnouts S., 1996, A&AS, 117, 393
Blagorodnova N., et al., 2017, The Astrophysical Journal, 844, 46
Blagorodnova N., et al., 2019, ApJ, 873, 92
Blanton M. R., Roweis S., 2007, The Astronomical Journal, 133, 734
Bricman K., Gomboc A., 2020, The Astrophysical Journal, 890, 73
Chen X., Madau P., Sesana A., Liu F. K., 2009, The Astrophysical Journal, 697, L149
Chornock R., et al., 2014, The Astrophysical Journal, 780, 44
Conroy C., Gunn J. E., White M., 2009, The Astrophysical Journal, 699, 486
Curran P. A., 2014, arXiv: Instrumentation and Methods for Astrophysics
Dong S., Bose S., Chen P., Brink T. G., de Jaeger T., Filippenko A. V., Zheng W., 2018, The Astronomer's Telegram, 12198, 1
Ferrarese L., Ford H., 2005, Space Sci. Rev., 116, 523
Fisher D. B., Drory N., 2008, The Astronomical Journal, 136, 773
Fletcher R., 1970, The Computer Journal, 13, 317
Foreman-Mackey D., Hogg D. W., Lang D., Goodman J., 2013, Publications of the Astronomical Society of the Pacific, 125, 306
French K. D., Arcavi I., Zabludoff A., 2016, The Astrophysical Journal Letters, 818, L21
Gebhardt K., et al., 2000, ApJ, 539, L13
Gezari S., 2021, ARA&A, 59
Gezari S., et al., 2006, The Astrophysical Journal Letters, 653, L25
Gezari S., et al., 2008, The Astrophysical Journal, 676, 944
Gezari S., Chornock R., Rest A., 2012, Nature, 485, 217–220
Gezari S., van Velzen S., Perley D. A., Hung T., Cenko S. B., Frederick S., Graham M., Kulkarni S. R., 2019, The Astronomer's Telegram, 12789, 1
Graur O., French K. D., Zahid H. J., Guillochon1 J., Mandel K. S., Auchettl K., Zabludoff A. I., 2018, The Astrophysical Journal, 853, 39
Guillochon J., Nicholl M., Villar V. A., Mockler B., Narayan G., Mandel K. S., Berger E., Williams P. K. G., 2018, The Astrophysical Journal Supplement Series, 236, 6
Gültekin K., et al., 2009, ApJ, 698, 198
Hills J. G., 1975, Nature, 254, 295–298
Holoien T. W.-S., et al., 2014, Monthly Notices of the Royal Astronomical Society, 445, 3263–3277
Holoien T. W., et al., 2016a, Monthly Notices of the Royal Astronomical Society, 455, 2918–2935
Holoien T. W.-S., et al., 2016b, Monthly Notices of the Royal Astronomical Society, 463, 3813–3828
Hu J., 2008, Monthly Notices of the Royal Astronomical Society, 386, 2242–2252
Hung T., et al., 2017, The Astrophysical Journal, 842, 29
Hung T., et al., 2018, ApJS, 238, 15
Häring N., Rix H.-W., 2014, The Astrophysical Journal, 487, L89–L92
Ilbert O., et al., 2009, The Astrophysical Journal, 690, 1236
Ivezić Ž., et al., 2019, ApJ, 873, 111
Kaiser N., et al., 2010, in Stepp L. M., Gilmozzi R., Hall H. J., eds, Society of Photo-Optical Instrumentation Engineers (SPIE) Conference Series Vol. 7733, Ground-based and Airborne Telescopes III. p. 77330E, doi:10.1117/12.859188
Khabibullin I., Sazonov S., Sunyaev R., 2013, Monthly Notices of the Royal Astronomical Society, 437, 327–337
Kochanek C. S., et al., 2017, Publications of the Astronomical Society of the Pacific, 129, 104502
Kormendy J., Ho L. C., 2013, Annual Review of Astronomy and Astrophysics, 51, 511
Lacy J. H., Townes C. H., 1982, The Astrophysical Journal, 262, 120
Law-Smith J., Ramirez-Ruiz E., Ellison S. L., Foley R. J., 2017, The Astrophysical Journal, 850, 20
Leja J., Johnson B. D., Conroy C., van Dokkum P. G., Byler N., 2017, The Astrophysical Journal, 837, 170
MacLeod M., Guillochon J., Ramirez-Ruiz E., 2012, The Astrophysical Journal, 757, 134
McConnell N. J., Ma C.-P., 2013a, ApJ, 764, 184
McConnell N. J., Ma C.-P., 2013b, ApJ, 764, 184
Mitchell P. D., Lacey C. G., Baugh C. M., Cole S., 2013, Monthly Notices of the Royal Astronomical Society, 435, 87
Mockler B., Guillochon J., Ramirez-Ruiz E., 2019, The Astrophysical Journal, 872, 151
Moffat A. F. J., 1969, A&A, 3, 455
Nicholl M., et al., 2019a, Monthly Notices of the Royal Astronomical Society, 488, 1878
Nicholl M., et al., 2019b, The Astronomer's Telegram, 12752, 1
Nicholl M., et al., 2020, Monthly Notices of the Royal Astronomical Society, 499, 482–504
Rees M., 1988, Nature, 333, 523–528
Robotham A. S. G., Taranu D. S., Tobar R., Moffett A., Driver S. P., 2017, MNRAS, 466, 1513
Siebert M. R., Strasburger E., Rojas-Bravo C., Foley R. J., 2019, The Astronomer's Telegram, 13131, 1
Stone N. C., Metzger B. D., 2015, Monthly Notices of the Royal Astronomical Society, 455, 859–883
Stoughton C., et al., 2002, The Astronomical Journal, 123, 485
Tonry J. L., et al., 2018, PASP, 130, 064505
Tucker M. A., Huber M., Shappee B. J., Dong S., Bose S., Chen P., 2018, The Astronomer's Telegram, 11444, 1
Wevers T., van Velzen S., Jonker P. G., Stone N. C., Hung T., Onori F., Gezari S., Blagorodnova N., 2017, Monthly Notices of the Royal Astronomical Society, 471, 1694–1708
Wevers T., Stone N. C., van Velzen S., Jonker P. G., Hung T., Auchettl K., Gezari S., Onori F., 2019, Monthly Notices of the Royal Astronomical Society, 487, 4136
Zabludoff A. I., Zaritsky D., Huan Lin H., Tucker D., Hashimoto Y., Shectman S. A., Oemler A., Kirshner R. P., 1996, The Astrophysical Journal, 466, 104
van Velzen S., 2018, The Astrophysical Journal, 852, 72

van Velzen S., et al., 2011, The Astrophysical Journal, 741, 73
van Velzen S., et al., 2018, The Astronomer's Telegram, 12263, 1
van Velzen S. V., Gezari S., Ward C., Frederick S., Hammerstein E., Cenko S. B., 2019a, Transient Name Server AstroNote, 88, 1
van Velzen S., et al., 2019b, The Astronomer's Telegram, 12509, 1
van Velzen S., Gezari S., Hung T., Gatkine P., Cenko S. B., Ho A., Kulkarni S. R., Mahabal A., 2019c, The Astronomer's Telegram, 12568, 1
van Velzen S., et al., 2021, The Astrophysical Journal, 908, 26

APPENDIX A: ARCHIVAL PHOTOMETRIC DATA AND FITS

Figures A1 and A2 show the Prospector model fits produced for each TDE host galaxy.

APPENDIX B: APPENDIX B: PARAMETERS

Table B1 lists our full sample of host galaxies, their bulge to total mass ratios and posteriors of the Prospector model.

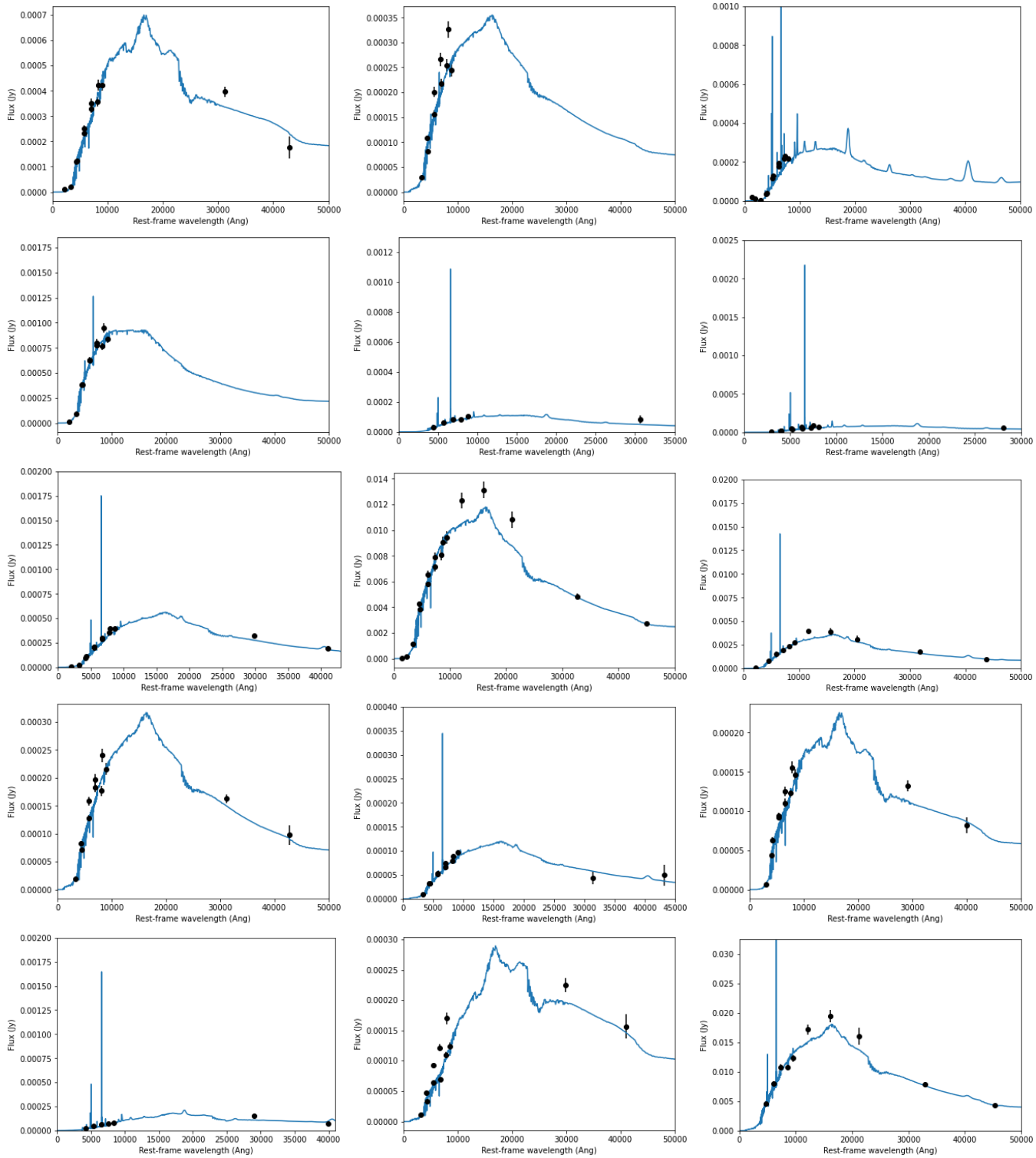

Figure A1. Archival photometry of each host galaxy (black) and the best fit model (blue), derived through Prospector. From left to right (1) AT2018zr (2) AT2018hco (3) AT2018iih (4) AT2018hyz (5) AT2018lna (6) AT2019cho (7) AT2019bhf (8) AT2019azh (9) AT2019dsg (10) AT2019ehz (11) AT2019eve (12) AT2019mha (13) AT2019meg (14) At2019lwu (15) AT2019qiz.

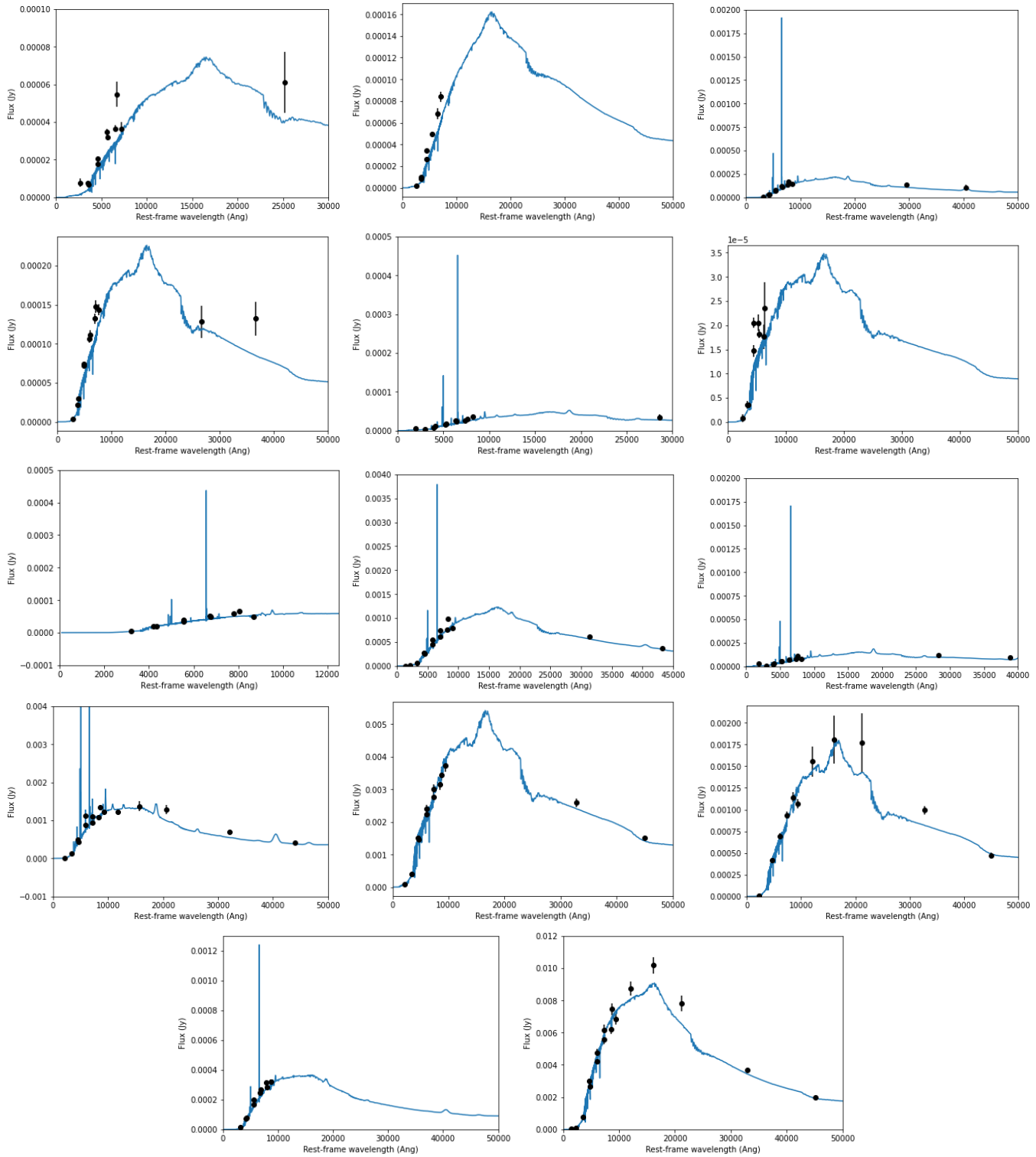

Figure A2. Archival photometry of each host galaxy (black) and the best fit model (blue), derived through Prospector. From left to right (16) GALEX-D1-9 (17) GALEX-D3-13 (18) SDSS-TDE1 (19) SDSS-TDE2 (20) PS1-10jh (21) PS1-11af (22) AT2017eqx (23) PTF-09ge (24) PTF-09djl (25) ASASSN14ae (26) ASASSN14li (27) ASASSN15oi (28) iPTF-16axa (29) iPTF-16fnl.

Table B1. Full TDE sample, with posterior medians and 1σ uncertainties from the Prospector model described in section 2.2 as well as B/T correction ratios discussed in section 1

TDE	$\log(M_{\rm total}/{\rm M}_\odot)$	(B/T)g	$\log(Z/{\rm Z}_\odot)$	ssfr50	sfr1	sfr2	sfr3	sfr4	sfr5	dust2	dust i	dust f
ASASSN-14ae	$9.94^{+0.15}_{-0.17}$	0.506±0.070	$-1.44^{+0.33}_{-0.39}$	$-10.25^{+0.19}_{-0.33}$	$0.19^{+0.31}_{-0.34}$	$0.14^{+0.29}_{-0.29}$	$0.12^{+0.32}_{-0.27}$	$0.11^{+0.32}_{-0.29}$	$0.07^{+0.31}_{-0.31}$	$0.62^{+0.10}_{-0.07}$	$-0.96^{+0.05}_{-0.03}$	$0.84^{+0.32}_{-0.32}$
ASASSN-14li	$9.78^{+0.07}_{-0.07}$	0.999±0.027	$0.01^{+0.09}_{-0.12}$	$-12.50^{+0.91}_{-0.71}$	$0.08^{+0.22}_{-0.25}$	$0.17^{+0.25}_{-0.24}$	$0.13^{+0.29}_{-0.31}$	$0.10^{+0.25}_{-0.27}$	$0.09^{+0.32}_{-0.31}$	$0.31^{+0.13}_{-0.11}$	$-0.57^{+0.15}_{-0.19}$	$1.02^{+0.29}_{-0.29}$
ASASSN-15oi	$9.25^{+0.10}_{-0.08}$	0.454±0.073	$0.01^{+0.12}_{-0.20}$	$-12.22^{+0.99}_{-0.88}$	$0.11^{+0.26}_{-0.29}$	$0.23^{+0.25}_{-0.29}$	$0.16^{+0.30}_{-0.29}$	$0.10^{+0.27}_{-0.26}$	$0.01^{+0.34}_{-0.31}$	$0.60^{+0.16}_{-0.12}$	$-0.79^{+0.19}_{-0.14}$	$1.00^{+0.30}_{-0.31}$
AT2017eqx	$9.56^{+0.11}_{-0.14}$	0.890±0.039	$-1.53^{+0.46}_{-0.33}$	$-10.57^{+0.52}_{-1.07}$	$-0.18^{+0.27}_{-0.24}$	$-0.04^{+0.30}_{-0.29}$	$-0.03^{+0.31}_{-0.29}$	$0.02^{+0.31}_{-0.27}$	$-0.02^{+0.29}_{-0.31}$	$0.48^{+0.15}_{-0.13}$	$-0.80^{+0.29}_{-0.14}$	$0.99^{+0.32}_{-0.29}$
AT2018hco	$10.18^{+0.09}_{-0.10}$	0.643±0.034	$-1.30^{+0.36}_{-0.45}$	$-11.77^{+0.93}_{-1.07}$	$-0.28^{+0.28}_{-0.27}$	$-0.16^{+0.24}_{-0.24}$	$-0.10^{+0.26}_{-0.26}$	$-0.05^{+0.30}_{-0.30}$	$-0.05^{+0.30}_{-0.30}$	$0.47^{+0.22}_{-0.19}$	$-0.25^{+0.36}_{-0.39}$	$0.99^{+0.33}_{-0.31}$
AT2018hyz	$9.84^{+0.09}_{-0.11}$	0.203±0.068	$-1.80^{+0.27}_{-0.13}$	$-11.32^{+1.06}_{-1.36}$	$0.18^{+0.26}_{-0.26}$	$0.22^{+0.28}_{-0.29}$	$0.18^{+0.30}_{-0.32}$	$0.12^{+0.29}_{-0.28}$	$-0.03^{+0.29}_{-0.27}$	$0.61^{+0.12}_{-0.10}$	$-0.95^{+0.07}_{-0.04}$	$1.02^{+0.29}_{-0.31}$
AT2018iih	$10.70^{+0.10}_{-0.15}$	0.690±0.107	$-1.47^{+0.72}_{-0.40}$	$-9.62^{+0.30}_{-0.28}$	$0.06^{+0.26}_{-0.31}$	$0.04^{+0.27}_{-0.26}$	$0.04^{+0.27}_{-0.25}$	$0.01^{+0.28}_{-0.29}$	$0.02^{+0.29}_{-0.32}$	$0.96^{+0.11}_{-0.09}$	$-0.94^{+0.09}_{-0.04}$	$0.86^{+0.26}_{-0.28}$
AT2018lna	$9.64^{+0.13}_{-0.14}$	0.521±0.074	$-1.31^{+0.52}_{-0.46}$	$-11.26^{+1.33}_{-1.58}$	$-0.03^{+0.28}_{-0.29}$	$-0.00^{+0.31}_{-0.30}$	$-0.02^{+0.30}_{-0.32}$	$-0.04^{+0.32}_{-0.32}$	$-0.04^{+0.30}_{-0.31}$	$0.64^{+0.25}_{-0.23}$	$-0.64^{+0.50}_{-0.27}$	$1.05^{+0.29}_{-0.27}$
AT2018zr	$9.96^{+0.10}_{-0.10}$	0.973±0.023	$0.04^{+0.12}_{-0.45}$	$-11.54^{+0.99}_{-1.06}$	$0.08^{+0.27}_{-0.28}$	$0.21^{+0.26}_{-0.29}$	$0.15^{+0.29}_{-0.29}$	$0.14^{+0.29}_{-0.30}$	$0.05^{+0.30}_{-0.31}$	$0.71^{+0.17}_{-0.16}$	$-0.78^{+0.38}_{-0.16}$	$1.00^{+0.28}_{-0.32}$
AT2019azh	$10.21^{+0.08}_{-0.07}$	0.798±0.051	$-0.79^{+0.10}_{-0.12}$	$-12.64^{+0.62}_{-0.59}$	$0.03^{+0.24}_{-0.21}$	$0.07^{+0.25}_{-0.28}$	$0.12^{+0.28}_{-0.31}$	$0.07^{+0.32}_{-0.26}$	$0.10^{+0.29}_{-0.29}$	$0.34^{+0.04}_{-0.03}$	$0.96^{+0.05}_{-0.03}$	$1.00^{+0.30}_{-0.29}$
AT2019bhf	$10.56^{+0.12}_{-0.15}$	0.529±0.043	$-0.83^{+0.36}_{-0.55}$	$-10.68^{+0.49}_{-0.93}$	$-0.04^{+0.27}_{-0.31}$	$-0.05^{+0.30}_{-0.31}$	$-0.08^{+0.28}_{-0.28}$	$-0.04^{+0.33}_{-0.31}$	$-0.07^{+0.31}_{-0.26}$	$0.73^{+0.22}_{-0.23}$	$-0.29^{+0.20}_{-0.27}$	$1.02^{+0.29}_{-0.34}$
AT2019cho	$10.04^{+0.13}_{-0.20}$	0.676±0.090	$-1.07^{+0.56}_{-0.60}$	$-9.63^{+0.40}_{-0.31}$	$-0.05^{+0.26}_{-0.28}$	$-0.00^{+0.32}_{-0.34}$	$0.04^{+0.29}_{-0.29}$	$0.03^{+0.30}_{-0.32}$	$0.04^{+0.28}_{-0.31}$	$0.69^{+0.12}_{-0.11}$	$-0.88^{+0.17}_{-0.09}$	$0.88^{+0.30}_{-0.26}$
AT2019dsg	$10.64^{+0.10}_{-0.11}$	0.271±0.074	$-1.10^{+0.33}_{-0.45}$	$-10.47^{+0.18}_{-0.22}$	$-0.10^{+0.28}_{-0.28}$	$-0.11^{+0.29}_{-0.28}$	$-0.08^{+0.27}_{-0.28}$	$-0.04^{+0.31}_{-0.30}$	$-0.01^{+0.31}_{-0.28}$	$0.77^{+0.16}_{-0.17}$	$-0.55^{+0.17}_{-0.22}$	$1.00^{+0.30}_{-0.28}$
AT2019ehz	$9.90^{+0.12}_{-0.17}$	0.676±0.057	$-1.03^{+0.42}_{-0.59}$	$-11.51^{+1.02}_{-1.25}$	$-0.08^{+0.27}_{-0.28}$	$-0.03^{+0.31}_{-0.25}$	$-0.03^{+0.28}_{-0.29}$	$-0.03^{+0.33}_{-0.28}$	$0.02^{+0.30}_{-0.31}$	$0.67^{+0.26}_{-0.21}$	$0.01^{+0.22}_{-0.35}$	$0.99^{+0.28}_{-0.30}$
AT2019eve	$9.31^{+0.09}_{-0.10}$	0.864±0.053	$-0.82^{+0.48}_{-0.76}$	$-11.00^{+0.63}_{-1.04}$	$-0.00^{+0.30}_{-0.28}$	$-0.09^{+0.32}_{-0.29}$	$-0.03^{+0.30}_{-0.30}$	$-0.02^{+0.28}_{-0.27}$	$-0.03^{+0.32}_{-0.32}$	$0.51^{+0.34}_{-0.31}$	$-0.16^{+0.29}_{-0.44}$	$1.00^{+0.31}_{-0.30}$
AT2019lwu	$10.09^{+0.09}_{-0.09}$	0.312±0.021	$0.06^{+0.09}_{-0.17}$	$-11.84^{+1.18}_{-1.10}$	$0.28^{+0.26}_{-0.27}$	$0.26^{+0.26}_{-0.27}$	$0.16^{+0.26}_{-0.31}$	$0.19^{+0.32}_{-0.31}$	$0.01^{+0.33}_{-0.28}$	$1.46^{+0.16}_{-0.15}$	$0.35^{+0.04}_{-0.06}$	$1.02^{+0.29}_{-0.33}$
AT2019meg	$10.16^{+0.12}_{-0.27}$	0.960±0.042	$-0.23^{+0.35}_{-0.60}$	$-9.73^{+0.55}_{-0.79}$	$-0.01^{+0.25}_{-0.28}$	$-0.01^{+0.31}_{-0.30}$	$0.02^{+0.29}_{-0.28}$	$0.01^{+0.29}_{-0.26}$	$0.04^{+0.31}_{-0.31}$	$1.22^{+0.26}_{-0.22}$	$0.25^{+0.11}_{-0.40}$	$0.84^{+0.32}_{-0.32}$
AT2019mha	$10.00^{+0.08}_{-0.08}$	0.564±0.068	$0.12^{+0.05}_{-0.08}$	$-11.79^{+1.04}_{-1.15}$	$0.10^{+0.24}_{-0.24}$	$0.30^{+0.27}_{-0.27}$	$0.30^{+0.27}_{-0.29}$	$0.17^{+0.33}_{-0.29}$	$0.08^{+0.33}_{-0.30}$	$0.48^{+0.11}_{-0.10}$	$-0.86^{+0.15}_{-0.10}$	$1.01^{+0.33}_{-0.31}$
AT2019qiz	$10.27^{+0.10}_{-0.12}$	0.160±0.084	$-0.90^{+0.26}_{-0.35}$	$-11.04^{+0.20}_{-0.30}$	$-0.13^{+0.27}_{-0.29}$	$-0.08^{+0.27}_{-0.27}$	$-0.06^{+0.29}_{-0.26}$	$-0.03^{+0.29}_{-0.26}$	$-0.03^{+0.28}_{-0.28}$	$0.59^{+0.17}_{-0.15}$	$-0.17^{+0.21}_{-0.28}$	$1.01^{+0.32}_{-0.30}$
D1-9	$10.50^{+0.11}_{-0.11}$	0.786±0.023	$-0.54^{+0.41}_{-0.68}$	$-12.15^{+1.05}_{-0.93}$	$0.18^{+0.29}_{-0.26}$	$-0.12^{+0.27}_{-0.26}$	$-0.05^{+0.28}_{-0.33}$	$-0.07^{+0.31}_{-0.26}$	$-0.00^{+0.29}_{-0.29}$	$0.54^{+0.35}_{-0.25}$	$-0.27^{+0.42}_{-0.44}$	$0.97^{+0.33}_{-0.30}$
D3-13	$11.02^{+0.17}_{-0.16}$	0.941±0.018	$-0.94^{+0.61}_{-0.61}$	$-11.74^{+1.05}_{-1.17}$	$-0.05^{+0.30}_{-0.30}$	$0.00^{+0.29}_{-0.28}$	$-0.10^{+0.29}_{-0.27}$	$-0.00^{+0.28}_{-0.28}$	$-0.04^{+0.27}_{-0.33}$	$1.27^{+0.44}_{-0.41}$	$0.06^{+0.23}_{-0.29}$	$1.01^{+0.28}_{-0.30}$
PS1-10jh	$9.68^{+0.12}_{-0.18}$	0.904±0.015	$-0.34^{+0.37}_{-0.69}$	$-9.95^{+0.56}_{-0.74}$	$-0.01^{+0.25}_{-0.27}$	$-0.02^{+0.25}_{-0.27}$	$-0.04^{+0.29}_{-0.32}$	$0.02^{+0.28}_{-0.35}$	$-0.04^{+0.29}_{-0.31}$	$0.61^{+0.34}_{-0.29}$	$0.05^{+0.24}_{-0.38}$	$1.00^{+0.28}_{-0.33}$
PS1-11af	$10.16^{+0.16}_{-0.13}$	0.806±0.061	$0.07^{+0.09}_{-0.15}$	$-12.06^{+0.95}_{-0.91}$	$0.08^{+0.29}_{-0.29}$	$0.24^{+0.27}_{-0.35}$	$0.22^{+0.34}_{-0.34}$	$0.11^{+0.37}_{-0.33}$	$0.08^{+0.32}_{-0.36}$	$0.43^{+0.15}_{-0.13}$	$-0.80^{+0.31}_{-0.15}$	$0.99^{+0.28}_{-0.27}$
PTF09djl	$10.36^{+0.13}_{-0.15}$	0.892±0.044	$-0.69^{+0.33}_{-0.81}$	$-9.62^{+0.20}_{-0.21}$	$-0.13^{+0.27}_{-0.26}$	$-0.11^{+0.27}_{-0.27}$	$-0.04^{+0.27}_{-0.30}$	$-0.09^{+0.30}_{-0.27}$	$-0.04^{+0.32}_{-0.30}$	$1.03^{+0.22}_{-0.21}$	$0.35^{+0.04}_{-0.06}$	$1.05^{+0.33}_{-0.33}$
PTF09ge	$10.33^{+0.10}_{-0.10}$	0.566±0.101	$-1.06^{+0.45}_{-0.57}$	$-11.12^{+0.52}_{-1.06}$	$0.00^{+0.28}_{-0.28}$	$-0.05^{+0.25}_{-0.28}$	$0.02^{+0.26}_{-0.29}$	$-0.04^{+0.29}_{-0.26}$	$0.01^{+0.29}_{-0.27}$	$0.80^{+0.23}_{-0.25}$	$-0.29^{+0.12}_{-0.22}$	$0.99^{+0.30}_{-0.28}$
TDE1	$10.21^{+0.12}_{-0.19}$	0.853±0.104	$-0.94^{+0.42}_{-0.60}$	$-10.10^{+0.43}_{-0.60}$	$-0.08^{+0.27}_{-0.26}$	$-0.09^{+0.37}_{-0.33}$	$-0.01^{+0.31}_{-0.29}$	$-0.03^{+0.29}_{-0.28}$	$0.02^{+0.28}_{-0.31}$	$0.82^{+0.21}_{-0.19}$	$-0.74^{+0.20}_{-0.18}$	$0.96^{+0.33}_{-0.28}$
TDE2	$10.66^{+0.12}_{-0.16}$	0.546±0.030	$-0.67^{+0.45}_{-0.49}$	$-11.34^{+1.10}_{-1.46}$	$-0.00^{+0.27}_{-0.29}$	$0.01^{+0.27}_{-0.29}$	$0.05^{+0.32}_{-0.28}$	$0.00^{+0.33}_{-0.34}$	$0.06^{+0.26}_{-0.30}$	$0.61^{+0.16}_{-0.18}$	$-0.84^{+0.18}_{-0.11}$	$0.98^{+0.31}_{-0.29}$
iPTF16axa	$10.31^{+0.11}_{-0.11}$	0.575±0.045	$-1.60^{+0.46}_{-0.28}$	$-11.39^{+0.98}_{-1.29}$	$-0.03^{+0.30}_{-0.30}$	$0.01^{+0.26}_{-0.27}$	$-0.04^{+0.32}_{-0.27}$	$0.08^{+0.25}_{-0.29}$	$0.04^{+0.28}_{-0.27}$	$0.80^{+0.16}_{-0.15}$	$-0.90^{+0.16}_{-0.07}$	$1.01^{+0.29}_{-0.33}$
iPTF16fnl	$10.12^{+0.05}_{-0.07}$	0.486±0.051	$-1.02^{+0.12}_{-0.12}$	$-13.14^{+0.48}_{-0.26}$	$-0.52^{+0.22}_{-0.24}$	$-0.26^{+0.25}_{-0.24}$	$-0.08^{+0.31}_{-0.29}$	$-0.10^{+0.31}_{-0.27}$	$-0.02^{+0.27}_{-0.28}$	$0.23^{+0.03}_{-0.03}$	$-0.95^{+0.08}_{-0.04}$	$1.02^{+0.24}_{-0.29}$

This paper has been typeset from a TEX/LATEX file prepared by the author.